Physics of Fluids

An automated method for the identification of interaction tone noise sources on the beamforming maps of counter-rotating rotors

Cite as: Phys. Fluids **34**, 047105 (2022); https://doi.org/10.1063/5.0083634
Submitted: 28 December 2021 • Accepted: 09 March 2022 • Published Online: 04 April 2022

B. Fenyvesi, J. Kriegseis and Cs. Horváth

COLLECTIONS

Paper published as part of the special topic on Flow and Acoustics of Unmanned Vehicles

ARTICLES YOU MAY BE INTERESTED IN

Physics of Fluids ARTICLE scitation.org/journal/phf

An automated method for the identification of interaction tone noise sources on the beamforming maps of counter-rotating rotors

Cite as: Phys. Fluids **34**, 047105 (2022); doi: 10.1063/5.0083634
Submitted: 28 December 2021 · Accepted: 9 March 2022 ·

B. Fenyvesi,[1,a)] J. Kriegseis,[2] and Cs. Horváth[1,b)]

AFFILIATIONS

[1]Budapest University of Technology and Economics, Faculty of Mechanical Engineering, Department of Fluid Mechanics, Műegyetem rkp. 3, 1111 Budapest, Hungary
[2]Karlsruhe Institute of Technology (KIT), Institute of Fluid Mechanics (ISTM), Kaiserstraße 10, 76131 Karlsruhe, Germany

Note: This paper is part of the special topic, Flow and Acoustics of Unmanned Vehicles.
[a)]**Author to whom correspondence should be addressed:** fenyvesi@ara.bme.hu
[b)]**Electronic mail:** horvath.csaba@gpk.bme.hu

ABSTRACT

Counter-rotating rotor configurations are considered more efficient than their single rotor counterparts. Consequently, the coaxially aligned rotors have appeared in the fixed-wing aircraft sector and are appearing in the quickly developing unmanned aerial vehicle sector, where they are expected to play a significant role, especially for long haul and heavy load configurations. As their noise levels have proven to be rather significant, the localization and reduction of the noise of such counter-rotating blade sets is a relevant topic of interest. One of the dominant contributors to counter-rotating rotor noise is interaction tones. Interaction tones appear at combinations of the harmonics of the blade passing frequencies of the two rotors and are significant throughout the spectra. In this paper, an automated method is presented that analyzes an entire series of beamforming noise source maps using principal component analysis-based methods in order to identify the dominant noise generation mechanisms in frequency bins that are associated with interaction tones. The processing technique is presented herein through the investigation of counter-rotating open rotor datasets developed for a fixed-wing aircraft configuration. With the proposed method, an objective mean has been provided for separating apart contributions from various noise sources, which can be automated, making the processing and investigation of large sets of measurement data rather quick and easy. The method has been developed such that the results of the analysis are easy to comprehend even without specialized prior knowledge in the area of counter-rotating rotor noise.

I. INTRODUCTION

This paper concerns the investigation of the interaction tone noise produced by counter-rotating rotor systems. Counter-rotating rotor systems consist of two coaxial rotors that rotate in opposite directions. The axis of the rotors can be aligned with either the horizontal or the vertical directions. While the horizontal alignment has been used in traditional fixed-wing aircraft technology, such as counter-rotating open rotor (CROR) aircraft engines, typical examples for vertical alignment or a combination of the two can be seen on multi-rotor unmanned aerial vehicles (UAV).

A significant amount of research has already been conducted for large-scale horizontal axis aircraft applications, with investigations dating back to as early as 1948.[1] It has been observed that the main benefit of counter-rotating rotors is the increase in efficiency as compared to single propellers and turbofan engines resulting from the reduction of swirl by the downstream propeller and their superior bypass ratios, that is, the ratio between the core and the bypass mass flow rates.[2–5] As UAVs are a rapidly growing technology driven by the wide range of applications including transportation, videography, delivery services, and many more, the idea that the use of counter-rotating rotors could increase their efficiency and lifting capacity has become increasingly relevant. However, it is also well-known that one of the main downsides associated with counter-rotating rotor applications is that they can be considerably louder than their single rotor counterparts.[1,6–14]

There have been numerous studies investigating the noise produced by counter-rotating configurations. It has been established in the early years of CROR-related research that interactions between the blade rows result in interference patterns.[1] Hanson,[3] Parry,[15] and Kingan[16] (among others) have developed analytical methods for understanding and predicting the noise of counter-rotating propellers. The effects of several design parameters have also been investigated in the past, such as various *RPM* (revolutions per minute) and blade pitch angle settings,[17] blade number configurations,[18] and the influence of various torque ratios.[19] Horváth *et al.* have used beamforming technology to localize and investigate the noise sources of counter-rotating open rotors,[10,11,20] applying a beamforming-based manual sorting method in order to categorize CROR noise sources.[12] In recent years, Tokaji *et al.*[21–23] and Fenyvesi *et al.*[24–26] have published studies in which they have used automated and semi-automated methods for the extraction and examination of various CROR noise components, aiming to significantly shorten the time needed to identify and subsequently analyze certain types of noise sources. Another significant advantage of these methods is that the different groups of noise sources can be identified and then investigated separately from each other. Most recently, Antoni *et al.*[27,28] have proposed a method for the extraction of cyclostationary tonal and broadband components from aeroacoustic signals, illustrating their method on CROR data.

Concerning UAV investigations, several studies have been published on the aerodynamics of counter-rotating UAVs (see Refs. 29–33, for example), and studies related to the acoustics thereof have also gained traction in the last few years. Liu *et al.*[34] have conducted a computational study on a micro UAV having counter-rotating propellers. They have found that tip–vortex interactions of the upstream with the downstream propeller have been a major noise source. Darvishpoor *et al.*[35] have published a review on different UAV applications, configurations, and flight mechanisms. They have divided UAVs into main and sub-categories and subsequently discussed the characteristics, advantages, and drawbacks of each category.

For example, McKay *et al.*[14] have presented a detailed experimental analysis of small UAVs equipped with counter-rotating propellers. They have found a large number of interaction tones in the spectrum, which are generally produced by the unsteady loading on the blades of each propeller due to their interaction with the unsteady flow from the other propeller. They have presented a simple theoretical model for predicting the interaction tones produced and have shown that the number of such tones can be reduced by the careful selection of the rotor blade numbers. In a separate study,[36] they have investigated the effects of different propeller diameters and spacings on counter-rotating UAV noise in hover mode. They have found that while the spectrum has also contained rotor-alone tones and broadband noise, interaction tones have been the main contributor to the overall noise level. Horváth *et al.* have provided design guidelines for counter-rotating blade sets based on the radiation efficiencies of the interaction tones of CRORs and have shown how they can be carried over to counter-rotating drone technology.[37]

A trend can also be observed when looking at the studies and their authors mentioned above. It can be seen that research groups for which the main focus has formerly been counter-rotating open rotor noise research are gradually shifting toward the investigation of counter-rotating UAVs, as there are several similarities between the design, fluid mechanics, and acoustics of the two.

In this paper, an automated method is presented which analyzes noise source maps in order to identify and subsequently categorize interaction tones, which are significant throughout the spectra. The proposed processing technique is presented herein through the investigation of a counter-rotating open rotor airplane engine dataset. Interaction tones are comprised of harmonics of the blade passing frequencies (BPF) of each rotor, as can be seen in Eq. (1). BPF_{F} and BPF_{A} refer to each of the counter-rotating rotors, with subscript "*F*" referring to the Forward, while subscript "*A*" referring to the Aft rotor. n_{F} and n_{A} are positive whole numbers, the harmonic indices of their respective rotors

$$f_{int} = n_F BPF_F + n_A BPF_A. \tag{1}$$

Noise source maps have been created from phased array measurement data using acoustic beamforming technology. In a phased array microphone system, a set number of microphones are positioned according to a well-defined pattern. Using the phase and amplitude differences between the recorded microphone signals, the direction of arrival of the acoustic wavefronts originating from sound sources can be estimated.[38] In presenting beamforming data, spatial noise source patterns pertaining to frequency bands (bins) of a given frequency range are visualized in the form of beamforming maps (BMs), making the localization of noise sources possible. The data are usually plotted using an appropriate dynamic range in order to show only the real and relevant noise sources in each frequency bin. Beamforming maps can then be examined both individually and as a series of beamforming maps in order to understand the underlying noise generation mechanisms, identify noise source groups, and examine their characteristics.

However, when a large frequency range needs to be broken down into sufficiently small frequency bins, the series of beamforming maps can be of considerable size, and the in-depth analysis of a dataset can be rather challenging. In the case of counter-rotating rotors, most of the tonal noise source groups are related to the rotation of the rotors, and thus, the frequencies associated with them. This can result in the presence of multiple (sometimes even spatially overlapping) noise sources in a frequency bin, which makes it hard to decide which noise source group to associate a given noise source pattern for further analysis.[11,12,38] In addition to the vast experience and knowledge required for the analysis of the underlying noise generation mechanisms, the time needed to examine up to several hundred noise source maps can be rather long.[12]

The identification and categorization of the noise sources associated with the interaction tones of counter-rotating rotors are also rather challenging. These noise sources are rotating coherent noise sources, for which the propagation of the coherent wavefronts coupled with their rotation about the axis results in a misleading resultant spiral wavefront, as the sound waves add up constructively and destructively. This has been visualized in the form of contour plots by Horváth *et al.*[10,20] with the help of the simulation of the sound field. The results have shown how the resultant spiral wavefronts of the circumferential spinning modes of rotating coherent noise sources interact with the microphones of the phased array, if the phased array is placed parallel to the axis of rotation. Consequently, as beamforming processes conventionally assume that the investigated noise sources are stationary and incoherent, they trace the resultant wavefronts of rotating coherent noise sources back to apparent noise source locations. These locations do not agree with the true locations of the rotating coherent noise source, but rather align with the so-called Mach radius.[15] It has also been established that the unique location of the Mach radius can be determined ahead of time for each individual interaction tone,[10,11,15] as will be seen later in the paper.

The method presented in this paper uses principal component analysis (PCA) methods to analyze the content of turbomachinery beamforming maps in order to find dominant noise source patterns, which can then be connected to noise source groups and pre-defined subgroups thereof. The basis of this novel method, combining PCA with beamforming, has also been developed by the authors of this paper.[24–26] In this investigation, the method has been further developed in order to make it capable of handling the specific challenges presented by the apparent noise source locations of interaction tones. The method provides an automated means for a quick and easy-to-use analysis of the beamforming maps of counter-rotating turbomachinery datasets while overcoming the above issues in order to identify and subsequently categorize interaction tone noise sources.

II. PRINCIPAL COMPONENT ANALYSIS

Principal component analysis is also known as Karhunen–Loève expansion[39,40] and proper orthogonal decomposition (POD).[41] It has been applied in various scientific fields, and it is especially useful for the recognition and separation of underlying patterns and major components in a large and complicated dataset. For example, it has been implemented in the analysis of molecular dynamics data,[42] meteorology,[43] and the investigation of complex velocity fields.[43–45] PCA has recently been used to analyze the radiated noise caused by turbulent flow/structure interaction,[46] and it has also been combined with wavelet-based beamforming methods in CPU cooling fan acoustic imaging for the investigation of a time series of beamforming maps at various frequencies of interest.[47]

PCA assumes that the phenomena under investigation can be explained by the variances and covariances between variables in the original dataset. It determines the characteristic degrees of freedom as contained in the underlying basis, which are referred to as the principal components or modes. In the context of beamforming map analysis, it has already proven to be a powerful tool for decreasing the time needed, and the amount of subjective judgment to be used in an analysis.[24–26]

Furthermore, if multiple information subgroups of the raw data basis can be determined, the extension of the general PCA to a common-base POD (CPOD) method allows for a quantitative comparison of these various subgroups in the dataset[48] When a dataset is processed with PCA and CPOD, information regarding the relative energy contributions of the pre-determined subgroups can be determined and associated with visual elements, such as spatial patterns of the original dataset. First, the background needed for understanding basic PCA will be presented, after which the specialized CPOD approach will be described.

Note, however, that only the main calculus steps are recapped in Sec. II A for brevity purposes, which build upon the chosen nomenclature of earlier manuscripts on beamforming[24–26] and other flow diagnostics[48–50] topics by the authors. For more comprehensive descriptions of POD, the reader is referred to hands-on tutorials[51,52] and comprehensive mathematical treatises[45,53,54] on the method.

A. Analytical description

In principal component analysis, the N input maps (i.e., BMs) of size $m = m_x \times m_y$ that comprise the input dataset under examination are to be described in vector form, $\mathbf{b}^{\mathbf{i}}$, $(i = 1 \ldots N)$. Each of the values in the vectors $\mathbf{b}^{\mathbf{i}}$ pertains to one single element from their respective input matrices of these maps. The N maps of length m are arranged in an $N \times m$ BM-matrix $\mathbf{Q}$,[51,55] that is,

$$\mathbf{Q} = \begin{bmatrix} \mathbf{b}^{\mathbf{1}} & \mathbf{b}^{\mathbf{2}} & \cdots & \mathbf{b}^{\mathbf{N}} \end{bmatrix}. \tag{2}$$

The BM-matrix $\mathbf{Q}$ [see Eq. (3)] is further converted into the (square) covariance matrix $\mathbf{R}$, according to

$$\mathbf{R} = \mathbf{Q}\mathbf{Q}^T, \tag{3}$$

for which the corresponding eigenvalue problem

$$\mathbf{R}\boldsymbol{\psi} = \boldsymbol{\lambda}\boldsymbol{\psi}, \tag{4}$$

is solved. The solution of the eigenvalue problem (4) provides the matrix

$$\boldsymbol{\psi} = \begin{bmatrix} \phi_1 & \phi_2 & \cdots & \phi_N \end{bmatrix}, \tag{5}$$

of eigenvectors ϕ_j and their corresponding λ_j eigenvalues

$$\boldsymbol{\lambda} = \begin{bmatrix} \boldsymbol{\lambda}_1 & 0 & \ldots & 0 \\ 0 & \boldsymbol{\lambda}_2 & & \vdots \\ \vdots & & \ddots & \vdots \\ 0 & \ldots & \ldots & \boldsymbol{\lambda}_N \end{bmatrix}, \tag{6}$$

which are arranged in decreasing order, that is, $\lambda_j > \lambda_{j+1}$.

In principal component analysis, the eigenvectors are referred to as the modes of the PCA, which are a set of orthogonal modes, and their respective eigenvalues convey how well each eigenvector captures the information contained in each map $\mathbf{b}^{\mathbf{i}}$ of the original dataset. The PCA modes can be visualized in the form of modal patterns a.k.a. PCA maps, through which—in the present context—the locations of the contributing noise patterns can be localized for each mode. In the PCA approach, the number of degrees of freedom does not change (given $N < m$), such that N input maps lead to N PCA modes.

As the modes are arranged in decreasing order according to their eigenvalues, the first few modes are the most important in terms of capturing the energy, that is, the information contained in the input dataset $\mathbf{Q}$. The relative contribution P_j of each mode j to the overall energy can be determined by normalizing the respective eigenvalues λ_j with the Euclidean norm of the eigenvalue matrix (6), that is,

$$P_j = \frac{\lambda_j}{||\boldsymbol{\lambda}||}. \tag{7}$$

Furthermore, the contribution of each of the PCA modes ϕ_j to the respective input maps $\mathbf{b}^{\mathbf{i}}$ is conveyed in terms of weighting coefficients a_j^i, which can be determined according to

$$a_j^i = \boldsymbol{\psi}\mathbf{b}^{\mathbf{i}} = \begin{bmatrix} {\phi_1}^T \mathbf{b}^{\mathbf{1}T} & {\phi_2}^T \mathbf{b}^{\mathbf{1}T} & \ldots & {\phi_N}^T \mathbf{b}^{\mathbf{1}T} \\ {\phi_1}^T \mathbf{b}^{\mathbf{2}T} & \ddots & & \vdots \\ \vdots & & \ddots & \vdots \\ {\phi_1}^T \mathbf{b}^{\mathbf{N}T} & \ldots & \ldots & {\phi_N}^T \mathbf{b}^{\mathbf{N}T} \end{bmatrix}. \tag{8}$$

This can be rewritten in order to highlight that each of the input maps can be expressed as a linear combination of the ϕ_j modes and their corresponding weighting coefficients $\mathbf{a}_{\mathbf{j}}^{\mathbf{i}}$ in the form of

$$\mathbf{b}^{\mathbf{i}} = \sum_{j=1}^{N} \mathbf{a}_{\mathbf{j}}^{\mathbf{i}} \phi_j = \boldsymbol{\psi}^T \mathbf{a}^{\mathbf{i}}. \tag{9}$$

The weighting coefficients can also be used to quantify the relationship between each individual input map ($\mathbf{b^i}$) to each of the individual modes (ϕ_j), as can be seen in the $\mathbf{a_j^i}$ weighting coefficient matrix on the right of Eq. (8). That is, each column of the weighting coefficient matrix gives information with regard to the contribution of one particular mode across the series of input maps, while each of the rows gives information on how the modes are linearly combined to describe one respective input map. Hence, the values of the weighting coefficients a_j^i serve as immediate measure to quantify the impact of mode ϕ_j in map b^i.

The $\boldsymbol{\mu}_\mathbf{j}^\mathbf{N}$ variance of the weighting coefficients of each mode across the N input matrices is calculated according to

$$\mu_j^N = \frac{1}{N}\sum_{i=1}^{N}(\mathbf{a_j^i})^2 \overset{\text{def}}{=} \frac{\lambda_j}{N}. \tag{10}$$

Equation (10) also shows that, by definition, the variance of any mode's coefficient across the N input matrices can also be calculated from its corresponding eigenvalue by dividing it by the total N number of matrices.

B. Expansion to the common-base processing (CPOD)

As it has been mentioned above, when the underlying basis of the raw data can be divided into multiple subgroups of information, a quantitative comparison between the subgroups is made possible by CPOD. The basic process is described in Ref. 48 by Kriegseis *et al.* through the investigation of spatial velocity fields. The CPOD-based post-processing of the input dataset allows for the quantification of the impact of pre-determined subgroups within the dataset under analysis, which are related to each other. Then, characteristic spatial patterns associated with the subgroups can be identified within the particular dataset.

Consider an experiment, in which a set number of particular subsets, *A*, *B*,… *Z*, of the original dataset have been determined. These subsets are comprised of the reduced number of input maps N^A, N^B,… N^Z. The sum $N^A + N^B + \cdots N^Z = N$ leads back to the total number of input maps considered. The relative energy contributions of the subsets to the modes are then derived from the sectional variances. Equation (11) presents the relative energy contribution for the contributing maps from the *A* subset, which can also be applied similarly for all the subsets considered. In accordance with Eq. (10) presented in Subsection II A, the sums of the sectional variances, by definition, add up to the eigenvalues of the respective modes divided by the number of input maps [see Eq. (12)]

$$\mu_j^{N^A} = \frac{1}{N^A}\sum_{A=1}^{N^A}(\mathbf{a_j^A})^2, \tag{11}$$

$$\mu_j^{N^A} + \mu_j^{N^B} + \cdots + \mu_j^{N^Z} = \mu_j^N \overset{\text{def}}{=} \frac{\lambda_j}{N}. \tag{12}$$

As a result of applying the CPOD-based processing method, an automated and objective means is provided for the identification and quantification of the contributions of particular pre-determined subsets to a dataset.

III. MEASUREMENT SETUP

The processing technique presented herein is demonstrated on a dataset from a counter-rotating open rotor airplane engine test campaign. The acoustic measurements have been carried out within the framework of a collaboration between general electric (GE) and NASA in the NASA Glenn Research Center 915-ft low-speed wind tunnel.[9–11,20] The open rotor propulsion rig used in the measurements allows for the independent setting of the rotational speeds and the blade angles of the two rotors. The 1/7th scale model has been equipped with the F31/A31 historical baseline blade set.[9] *F* and *A* will be used to refer to the two counter rotating rotors, the Forward and the Aft rotors, respectively. The forward rotor of this particular configuration has a diameter of $D_\mathrm{F} = 0.652\,\mathrm{m}$ and has $B_\mathrm{F} = 12$ blades, while the aft rotor has a diameter of $D_\mathrm{A} = 0.630\,\mathrm{m}$ and has $B_\mathrm{A} = 10$ blades. The test configuration investigated herein is that of the approach condition, which is characterized by blade angles of 33.5 and 35.7 on the forward and the aft rotors, respectively. Furthermore, the angle of attack of the flow with regard to the test rig has been set to 0, while the wind tunnel Mach number has been *Ma* 0.2.

Measurement test cases for five different *RPM*s are investigated in the present study. This presents the robustness of the method on multiple sets of data, while also highlighting the advantages of the automated method, which is able to process a vast amount of data in a short amount of time. This provides a large set of processed data, which can be compared as a function of the *RPM*. The *RPM* values on the two rotors have been set to predefined values of corrected standard day (*STD*) *RPM* for which the actual measured *RPM* values (RPM_F and RPM_A) can be found for all of the five test cases in the table presented in Fig. 1. The first operating condition is the design point (DP) for the approach condition with an *RPM* of 5598 1/min. The IDs of the test cases are given based on their corrected standard day *RPM* values, so that when looking at the results, one can draw conclusions based on the differences in test conditions, which can immediately be seen based on the *RPM* values.

A schematic drawing of the top view of the measurement setup can be seen in Fig. 2. The test configuration investigated herein is that of an isolated CROR (not having a pylon mount). As seen from the upstream direction (left-hand side), the forward rotor rotates in the clockwise direction, while the aft rotor rotates in the counterclockwise direction. It can also be seen that a phased array microphone system has been installed in a cavity of the wall of the facility, directly across from the open rotor test rig and behind an acoustically transparent Kevlar® sheet. This is meant to displace the boundary layer of the main flow from the surface (and hence the microphones) of the array. The Array48 system manufactured by OptiNAV consists of 48 flush-mounted Earthworks M30 microphones and an optical camera, which has been built into the center of the array plate. The distance between the center plane of the test rig and the plate of the phased array has been $L = 1.6\,\mathrm{m}$. Measurements have been carried out for a sampling time of 45 s at a sampling frequency of 96 kHz. The optical camera built into the array has been used to capture the field of view of the array. This photo has been used during the data processing phase in order to superimpose the noise source maps on the image of the measured CROR configuration. Further details regarding the measurement setup can be found in the various publications related to the research test campaign.[9–11,20]

IV. THE DATASET

Functional beamforming[56] has been carried out on the phased array microphone datasets of the five CROR test cases through which

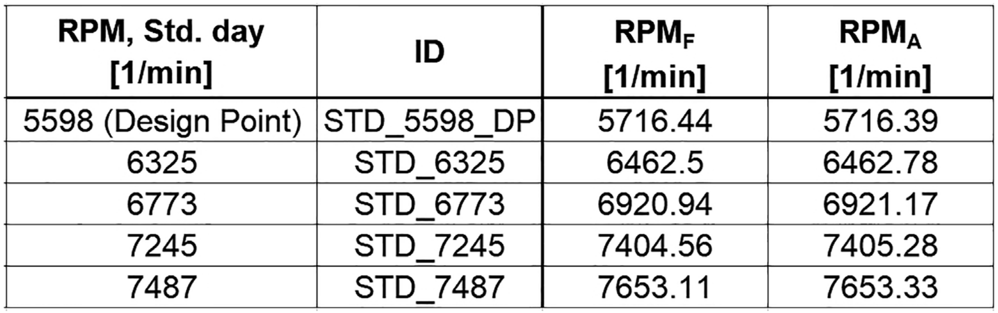

RPM, Std. day [1/min]	ID	RPM_F [1/min]	RPM_A [1/min]
5598 (Design Point)	STD_5598_DP	5716.44	5716.39
6325	STD_6325	6462.5	6462.78
6773	STD_6773	6920.94	6921.17
7245	STD_7245	7404.56	7405.28
7487	STD_7487	7653.11	7653.33

FIG. 1. *RPM* values for the five investigated CROR test cases.

the proposed processing technique is presented. Custom bandwidths have been utilized in order to divide the frequency range between each BPF of the aft rotor (BPF_A) into 50 equal bins. The investigated frequency range starts at the first BPF_A and ends at the tenth As a result, five input datasets, each of them containing 451 beamforming maps, have been produced. This choice of bandwidth allows for a simple comparison between the various cases, as investigated interaction tones will fall in the same bin for each case.

Example results of beamforming maps and their locations on the spectrum are shown in Fig. 3 at various interaction tone frequencies for test configuration *STD_5598_DP*. At the top of the figure, the power spectral density (PSD) spectrum of the BeamForming peak (BFpeak) values, that is, the maximum beamforming values on each beamforming map of a given case is shown. The BFpeak values for the PSD spectrum have been calculated from the maximum values on the $\mathbf{b}^{\mathbf{i}}$ beamforming maps [see Eq. (13)] considering the custom Δf bandwidths, which have been utilized in order to divide the frequency range between each BPF of the aft rotor (BPF_A) into 50 equal bins. The values of the Δf bandwidths are dependent on the *RPM*s corresponding to the various test cases, with all of the values being close to 20 Hz

$$BFpeak = max(b^i) - 10lg(\Delta f). \tag{13}$$

It can be seen on the horizontal axis of the spectrum that the frequency is given as a function of the BPF_A. Subplots (a)–(e) of Fig. 3 show the beamforming maps of the selected frequency bins marked with red circles on the spectrum. The beamforming maps are cropped so that only the vicinity of the rotors is shown. The CROR is outlined in order to help distinguish it from the background. The beamforming noise source patterns are superimposed over the measurement setup. The beamforming maps are plotted using a dynamic range of 4 dB with respect to the BFpeak values of the individual maps, so that the displayed values show the most dominant noise source (or noise sources) of the investigated frequency bin. The value of the BFpeak is given above each map next to the name of the interaction tone with which it is associated [see the formula in Eq. (1)].

It has been mentioned above that the beamforming process generally assumes that the investigated noise sources are stationary and incoherent, therefore localizing rotating coherent noise sources (i.e., interaction tones and BPF noise sources) to apparent noise source locations. The apparent locations do not agree with the true locations of the noise sources, but rather align with their so-called Mach radii when investigated from sideline locations, as in this investigation.[10,11,15] The red lines drawn on the beamforming maps of Fig. 3 display the calculated positions of the Mach radii pertaining to the interaction tones associated with the selected frequency bins. It can be seen that in some cases beamforming has localized the apparent noise sources near the axis within the hub instead of somewhere on the blades. In other cases, the apparent noise sources have been localized outboard of the blade tip. In addition, in every selected case presented in this figure, there has been a significant noise source localized to the Mach radius associated with the given frequency bin. It should be noted that many beamforming methods have been tested by Horváth *et al.*,[10] and it has been found that all of the methods provide similar results, not being able to localize the rotating coherent noise sources to their true locations.

The equation for calculating the Mach radius (z^*) is given in Eq. (14), where $z^* = 0$ refers to the axis of the rotor, while the radial location $z^* = 1$ refers to the blade tip. As has been established above, n is the harmonic index. The subscripts of n refer to the rotors of the acoustic (1) and the loading (2) harmonic, as in the case of CRORs

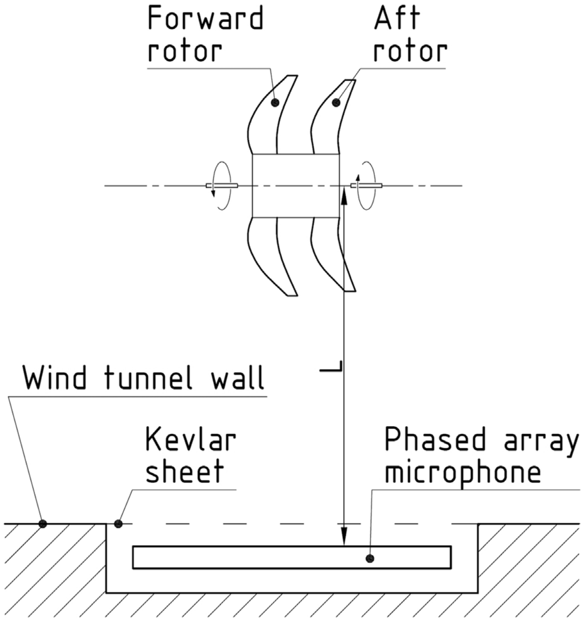

FIG. 2. Schematic drawing of the measurement setup—top view.

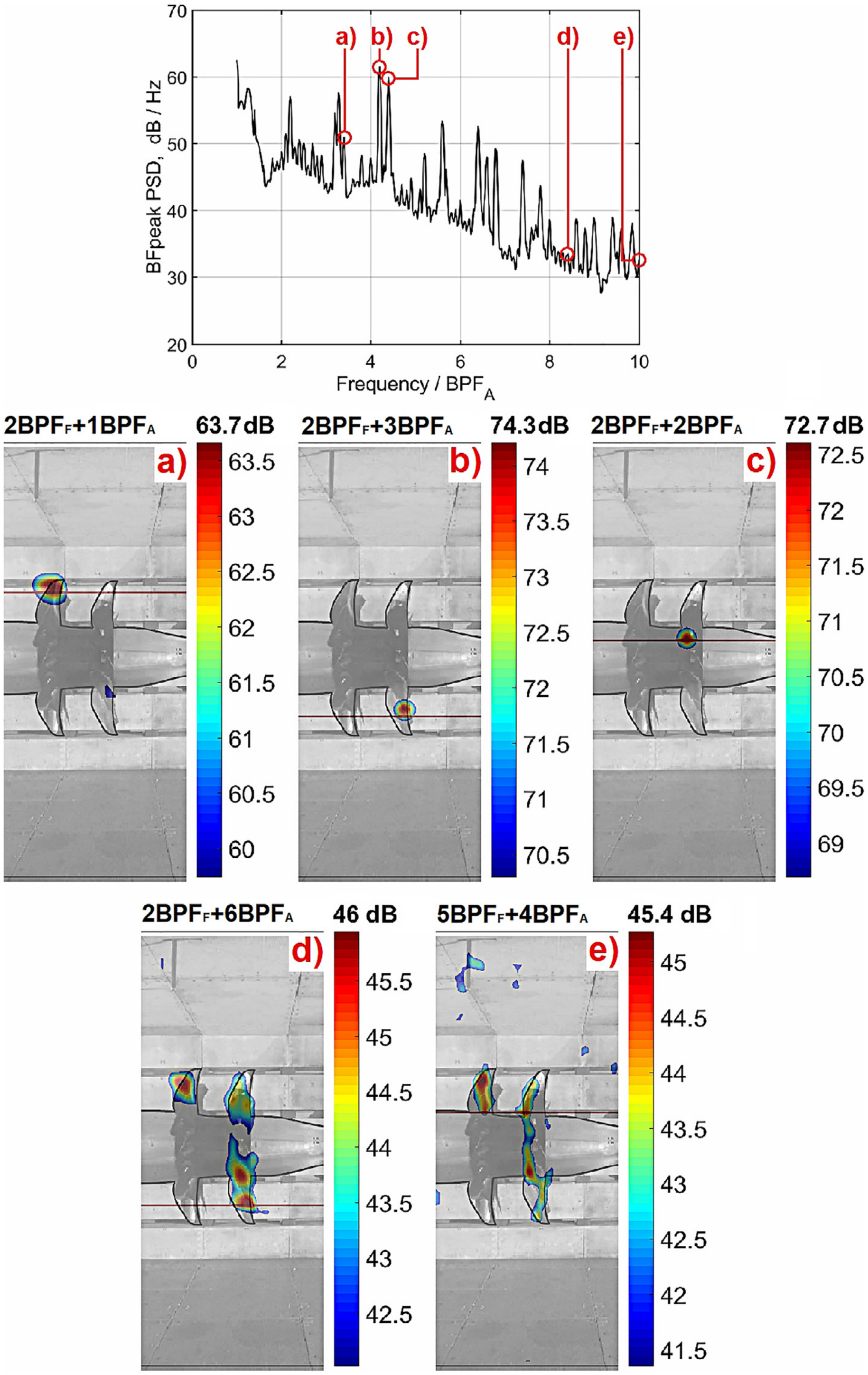

FIG. 3. Example beamforming results at various interaction tone frequencies: (a) 2 BPF_F+1 BPF_A; (b) 2 BPF_F+3 BPF_A; (c) 2 BPF_F+2 BPF_A; (d) 2 BPF_F+6 BPF_A; and (e) 5 BPF_F+4 BPF_A.

there is generally a sound radiating from one blade row (acoustic harmonic), which is loaded by the other blade row (loading harmonic).[3,15,57] As each blade row loads the other blade row while also radiating sound simultaneously, both rotors need to be considered as acoustic as well as loading harmonics. Therefore, it is important to determine the possible sources of loading in order to have a good understanding of the noise source. B refers to the blade count of the respective rotors, and M_t is the blade tip Mach number, while M_x is the flight Mach number, and θ is the angle of the observer with regard to the flight axis (see Fig. 4). A positive Mach radius value refers to the side of the axis on which the rotor is spinning toward the observer

$$z^* = \frac{n_1B_1 - n_2B_2}{n_1B_1M_{t_1} + n_2B_2M_{t_2}} \frac{1 - M_x \cos\theta}{\sin\theta}. \tag{14}$$

It has to be noted that prior to the determination of the Mach radius, the subject of multiple interaction tones in a given frequency bin needs to be addressed. As the interaction tones are comprised of the combined harmonics of the blade passing frequencies of the counter-rotating rotors, it is possible that multiple combinations fall in given bins at higher frequencies. As an example, take the combinations $1BPF_{\mathrm{F}} + 7BPF_{\mathrm{A}}$ and $6BPF_{\mathrm{F}} + 1BPF_{\mathrm{A}}$, which both give back the interaction tone frequency value of 7812 Hz in the case of measurement test case *STD_5598_DP*. The Mach radii for these interaction tones are different [see Eq. (14)], and only one interaction tone can be investigated for each of the *N* numbers of maps, and therefore, it has to be determined which one can be expected to be the dominant one to be considered for further calculations. It can be expected based on earlier findings that the one which radiates with a larger efficiency toward the direction of the observer (hence in the azimuthal direction toward the phased array) will have the largest peaks associated with it on the beamforming maps.[10,57] It has been shown in the literature[57–59] that the value of the radiation efficiency is dependent on the value of the azimuthal mode number. The azimuthal mode number, m, is equal to the number of lobes rotating around the axis for the given mode. It can be calculated using the harmonic indices (n) and the number of blades on the rotors (B) according to the formula shown in Eq. (15)

$$m = |n_1B_1 - n_2B_2|. \tag{15}$$

The investigations in the literature have shown that as the absolute value of the azimuthal mode number of an interaction tone is increased, its radiation efficiency will decrease.[57–59] Therefore, the radiation efficiency for an interaction tone is proportional to the value of $1/m$. Consequently, in the case of multiple interaction tones present in a frequency bin, the one with the largest $1/m$ needs to be considered, as it will most likely be the dominant one.

In order to help one understand the significance of the locations of the various Mach radii, the plane of the rotor under investigation can be subdivided into four quadrants, as has been proposed in Ref. 11. These quadrants can be seen in Fig. 5. The axis of the CROR splits the investigated area into a top and a bottom half, while a line between the forward and aft rotors splits the plane into forward and aft sections. The names of the quadrants correspond to the signs of the Mach radii in the given quadrants, and the rotors they are associated with. Their abbreviations are as follows: positive forward (*PF*), negative forward (*NF*), negative aft (*NA*), and positive aft (*PA*).

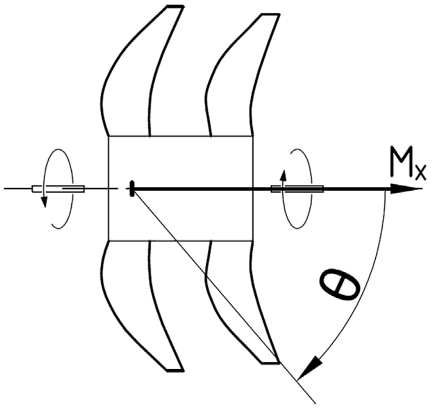

FIG. 4. The counter-rotating open rotor configuration and variables used in calculating the Mach radius.

As can be seen in Eq. (14), the relationship between the products of the harmonic indices and the blade counts ($n_{\mathrm{F}}B_{\mathrm{F}}$ and $n_{\mathrm{A}}B_{\mathrm{A}}$) is important in the Mach radius calculation. For $n_{\mathrm{F}}B_{\mathrm{F}} < n_{\mathrm{A}}B_{\mathrm{A}}$, the value of the Mach radius will be negative on the forward rotor and positive on the aft rotor. This will place the Mach radius (and the corresponding rotating coherent noise source) below the axis for this view. On the other hand, in the case of $n_{\mathrm{F}}B_{\mathrm{F}} > n_{\mathrm{A}}B_{\mathrm{A}}$ the Mach radius will be positive on the forward rotor and negative on the aft rotor, placing it above the axis for this view.

Based on their investigations of directivity patterns resulting from the loading of the potential flow fields, Parry and Crighton[15] have shown that when $n_{\mathrm{F}}B_{\mathrm{F}} < n_{\mathrm{A}}B_{\mathrm{A}}$, the louder noise source will be associated with the aft rotor, while in the case of $n_{\mathrm{F}}B_{\mathrm{F}} > n_{\mathrm{A}}B_{\mathrm{A}}$, the louder noise source will be associated with the forward rotor. Furthermore, as the aft rotor is located downstream of the forward rotor, the viscous wake of the forward rotor also has an effect on the noise of the CROR. It also has to be noted that according to the above conditions, the *NF* quadrant will not contain a dominant noise source in the case of the present CROR configuration, which has also been described by Horváth.[11] It has been stated previously that the value of the Mach radius can only be negative on the forward rotor in the case of $n_{\mathrm{F}}B_{\mathrm{F}} < n_{\mathrm{A}}B_{\mathrm{A}}$ [see Eq. (14)]. On the other hand, it has been determined by Parry and Crighton[15] that in this case the louder noise source will be associated with the aft rotor and hence the *PA* quadrant instead of the *NF* quadrant.

Therefore, the quadrant, with which a particular interaction tones apparent noise source is associated with, provides significant information regarding the true source of the noise. It can be seen on the example beamforming maps in Fig. 3 that in most cases a stronger noise source is associated with either the forward or the aft rotor. If the dominant interaction tone noise source is localized to the Mach radius associated with the *PF* or *NF* quadrants, then the dominant interaction tone noise source is the potential flow field of the aft rotor interacting

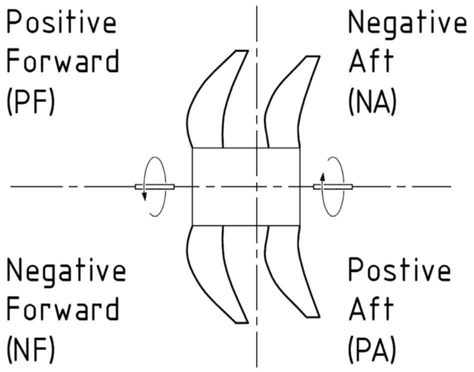

FIG. 5. Beamforming map quadrants according to the Mach radii.

with the forward rotor, while for quadrants *NA* and *PA*, the potential flow field of the forward rotor combined with the viscous wake of the forward rotor is the dominant source of loading.[11]

For the example results shown in Fig. 3, the red lines drawn on the beamforming maps display the calculated positions of the Mach radii pertaining to the interaction tones associated with the given frequency bins. If the line intersects with the dominant noise source of the frequency bin, then it is most likely a rotating coherent noise source. However, as it can be seen in Fig. 3, this manual identification process is not always straightforward, as the dominant noise source is not a concentrated "spot" in every case, but can have a spatially scattered shape, which could be associated with other noise sources, such as broadband noise sources.[10–12]

Therefore, the CPOD-based processing method presented herein aims to provide an automated, quick, and objective means for identifying the frequency bins and subsequently the beamforming map quadrants dominated by the interaction tones of counter-rotating rotor datasets. Note that while the formula in Eq. (14) adequately predicts the locations of the apparent noise sources, the red line does not always pass through the exact center of the BFpeak. This phenomenon has been investigated in detail by Horváth *et al.*,[10] and it has been found that these slight uncertainties are mainly associated with the phased array and the simplifications that have been made to derive the above formula for the Mach radius.

V. DEVELOPMENT OF THE CPOD APPROACH FOR THE INVESTIGATION OF INTERACTION TONES

It has been established so far in the present paper, that when multiple large datasets of beamforming maps are to be examined, it could be a rather challenging task to analyze them. There can be multiple noise source groups acting with different generation mechanisms and various further attributes to consider. It has also been presented that PCA can be used to identify the principal components of a dataset in order to create a representation of it that makes it possible to determine and subsequently investigate categories or modes of the underlying problem. Furthermore, it is possible to calculate the contribution of each input map to each of the modes and vice versa. Subgroups of the original dataset can also be determined, which can be useful when multiple noise source groups and mechanisms are to be considered for investigation. Then, CPOD can be used to investigate the effect of predetermined map subgroups on the modes of the dataset. The basic analysis of the combined method[24–26] is further developed keeping in mind the unique attributes of interaction tone noise sources of counter-rotating rotors such as UAVs or CRORs presented above, in order to make it possible to identify and subsequently categorize them in an objective and automated manner. Therefore, the subgroups investigated by the CPOD process are to be the aforementioned quadrants of interaction tones (see Sec. IV).

The implementation of the CPOD approach is presented through the example of the analysis of the CROR measurement test case *STD_5598_DP* (see Sec. III). In Sec. VI, the measurement test cases presented in Fig. 1 will be analyzed. As a summary of the steps of the identification process, a flow chart has been created, which can be seen in Fig. 6. The steps have been sorted into main subgroups, in order to make it easier to follow the process. These are marked with different colors in the flow chart of Fig. 6.

In order to obtain the dataset for the investigation, measurement data are to be collected using a phased array microphone system and a side-view configuration of the counter-rotating system as can be seen in Fig. 2. Then, beamforming in the frequency domain has to be carried out on the phased array microphone data in order to create beamforming maps (see steps 1 and 2 marked with gray color in the flow chart of Fig. 6). As the current goal is to investigate interaction tones only, which can be associated with distinct frequency bins, the interaction tone frequencies are to be calculated and the frequency bins associated with them are to be identified (see step 3 in Fig. 6). From here on, only the beamforming maps associated with these pre-determined interaction tone frequency bins are to be analyzed.

It has been presented in Sec. IV that the radiation efficiency for an interaction tone is proportional to the value of the reciprocal of the azimuthal mode number, $1/m$ [see Eq. (15)]. Therefore, the $1/m$ values are to be calculated for each interaction tone (see step 4 in Fig. 6). When multiple interaction tones are present in a frequency bin, in order to determine which interaction tone will most likely be dominant, the one with the largest $1/m$ value needs to be considered for further investigations (see step 5 in Fig. 6).

As it has been determined which interaction tone is to be considered for each of the frequency bins, the Mach radii according to Eq. (14) can be calculated for all of the interaction tones considered (see Step 6) in Fig. 6). Then, as it has been described in Sec. IV, the quadrants $(PF, NF, PA, \text{and}\ NA)$, in which each of the interaction tone noise sources is expected to be, can be determined based on the signs of the Mach radii and the relationships between the products of the harmonic indices and the blade counts, that is, $n_\mathrm{F}B_\mathrm{F}$ and $n_\mathrm{A}B_\mathrm{A}$ (see step 7 in Fig. 6).

It has also been established in Sec. IV that the locations of the apparent noise sources, and hence the Mach radii, are different for every interaction tone, which makes it difficult for the PCA-based method to identify reoccurring noise patterns. Therefore, a spatial rearrangement technique for rearranging the beamforming maps has been developed and applied herein. The process is shown in Fig. 7. The red lines drawn on the beamforming maps display the calculated positions of the Mach radii pertaining to the dominant interaction tones associated with the given frequency bins. For demonstrational purposes, maps having dominant noise sources that coincide with the Mach radii (thus the interaction tone noise sources are dominant) have been selected for both examples in Fig. 7. The goal is to shift the locations of the Mach radii to two possible predefined radial locations, which are significantly outboard of the blade tip (above or below the axis of the counter-rotating rotors), where no other categories of noise sources are localized and they are also not spatially interfering with each other. The blue lines drawn on the maps in Fig. 7 display these pre-determined locations. In the case of the beamforming maps for which the Mach radii are below the axis, the locations of the Mach radii are shifted to the predefined outboard location below the axis [see subplot (a) of Fig. 7], while in the case of the Mach radii being above the axis, the locations of the Mach radii are shifted to the same outboard location above the axis [see subplot (b) of Fig. 7]. The above process can be seen in step 8 in Fig. 6.

Then, according to the description presented in Sec. II, the input beamforming maps to the PCA and CPOD analyses are to be given in vector form. The vectors are referred to as the beamforming vectors $\mathbf{b}^\mathbf{i}, (i = 1\ldots N)$, the elements of which are the beamforming values of

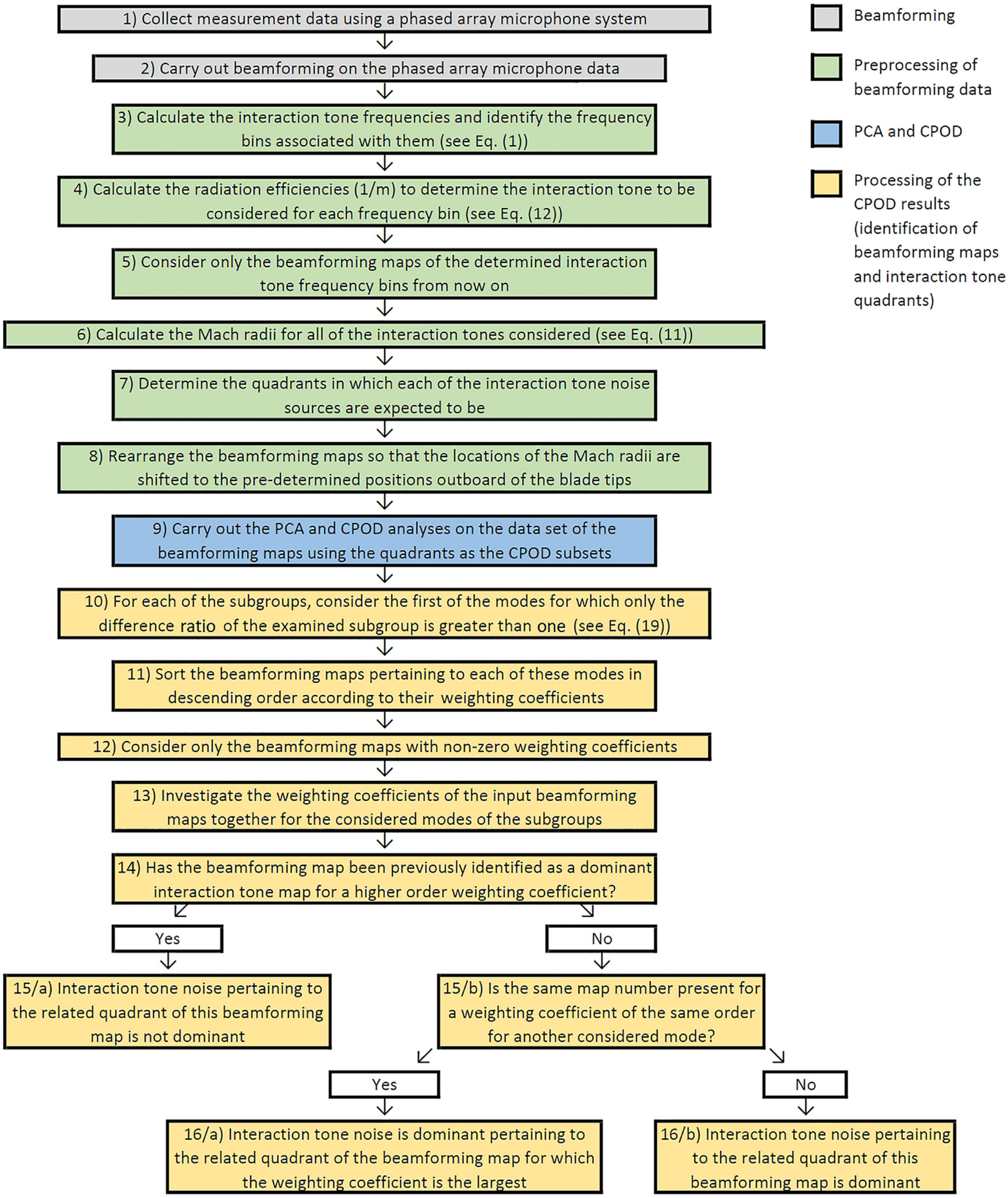

FIG. 6. Flow chart of the method.

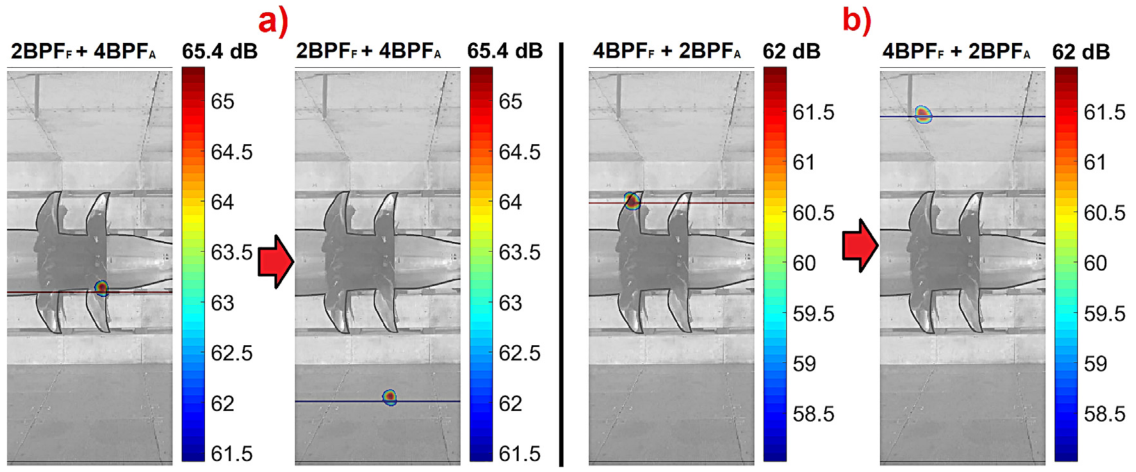

FIG. 7. The Mach radii (red lines) of the beamforming maps are shifted to predefined outboard positions (blue lines): (a) 2 BPF_F+4 BPF_A; and (b) 4 BPF_F+2 BPF_A.

their respective (rearranged) noise source maps, with each value pertaining to a grid point of the inspected acoustic field. Then, the PCA and CPOD analyses are to be carried out on the dataset comprised of the beamforming maps, defining the interaction tone quadrants as the subsets of the CPOD process. Therefore, the four subsets are comprised of different numbers of source maps N^{PF}, N^{NF}, N^{PA}, and N^{NA}, where the superscripts denote the subgroups of the four different quadrants in which the interaction tones are expected to be as presented in Fig. 5. As only frequency bins of interaction tones have been considered, the sum $N^{PF} + N^{NF} + N^{PA} + N^{NA} = N$ leads back to the total number of interaction tone input matrices considered (as N input maps lead to N PCA modes). The sectional variances, from which the relative energy contributions of the subsets to the modes are calculated from, are presented in Eqs. (16)–(19). The sums of the sectional variances add up to the eigenvalues of the respective modes divided by the number of input matrices [see Eq. (20)]. The PCA and CPOD analyses are addressed in the flow chart of Fig. 6 in step 9:

$$\mu_j^{N^{PF}} = \frac{1}{N^{PF}} \sum_{PF=1}^{N^{PF}} \left(\mathbf{a}_j^{\mathbf{PF}}\right)^2, \tag{16}$$

$$\mu_j^{N^{NF}} = \frac{1}{N^{NF}} \sum_{NF=1}^{N^{NF}} \left(\mathbf{a}_j^{\mathbf{NF}}\right)^2, \tag{17}$$

$$\mu_j^{N^{PA}} = \frac{1}{N^{PA}} \sum_{PA=1}^{N^{PA}} \left(\mathbf{a}_j^{\mathbf{PA}}\right)^2, \tag{18}$$

$$\mu_j^{N^{NA}} = \frac{1}{N^{NA}} \sum_{NA=1}^{N^{NA}} \left(\mathbf{a}_j^{\mathbf{NA}}\right)^2, \tag{19}$$

$$\mu_j^{N^{PF}} + \mu_j^{N^{NF}} + \mu_j^{N^{PA}} + \mu_j^{N^{NA}} = \mu_j^{N} \overset{\text{def}}{=} \frac{\lambda_j}{N}. \tag{20}$$

Furthermore, it is important to be able to identify whether a noise pattern occurs predominantly due to an investigated noise source group. Therefore, according to the principles established by the authors when describing the basic methodology of the analysis,[24–26] the concept of the energy ratio of the sectional variances is to be used when examining each of the subsets. For example, in the case of the *PF* subset the energy ratio for a given j mode is the sectional variance of the *PF* subset divided by the variance of the whole mode ($\mu_j^{N^{PF}}/\mu_j^N$). Then, the calculated energy ratio can be compared to the value of the expected evenly distributed contribution N^{PF}/N of the subset, which is a known value from the initial interaction tone calculations. Consequently, the energy ratio values above or below this value of expected contribution indicate whether the respective modal noise patterns in a CPOD mode are related to the interaction tone noise pattern of the given quadrant or not.

The d_c difference ratio is introduced, which is the ratio of the relative energy contributions (energy ratios) of the subsets and the values of their expected contributions [see Eq. (21)]. This information can then be used to determine the modes that are to be looked at in order to visualize the relative impacts of the subsets and subsequently identify the noise source patterns associated with the interaction tone quadrants. Suppose that the d_c difference ratio associated with the quadrant of the *PF* subset is above 1 for a given mode. In that case, it can be stated that the spatial noise patterns of the input beamforming maps initially associated with the *PF* frequency bins have had an effect, which is larger than expected for that mode. Furthermore, a non-zero difference ratio, which is below 1, can also indicate that the input map has had some effect on the mode, but it is of minor importance for the given subset

$$d_c = \frac{\dfrac{\mu_j^{N^{PF}}}{\mu_j^{N}}}{\dfrac{N^{PF}}{N}}. \tag{21}$$

It has been established by the authors in earlier studies that the first few modes usually contain the majority of the energy that can be found in the dataset.[24–26] Therefore, upon investigating several datasets during the present study, it has been determined that for each of the interaction tone subgroups (i.e., quadrants), the first of the modes are to be considered for which only the d_c ratio of the examined subgroup is greater than one, while the d_c ratios corresponding to the other subsets are below it (see step 10 in Fig. 6).

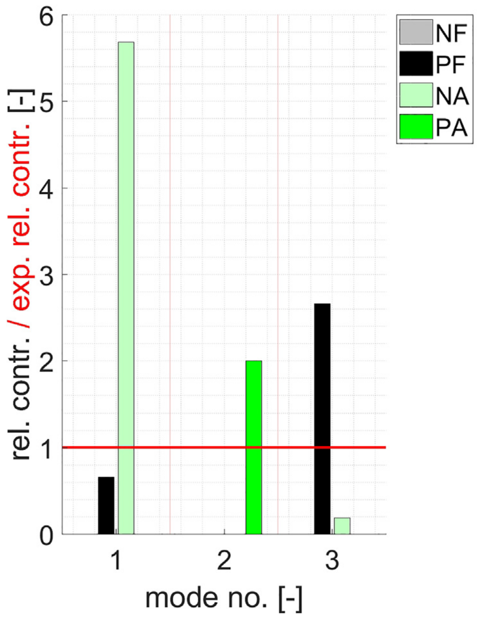

FIG. 8. Difference ratios of the relative energy contributions of the subsets from the values of their expected contributions.

Information with regard to the d_c difference ratio of the relative energy contributions of the subsets from the values of their expected contributions ([see Eq. (21)] is given in the form of bar plots in Fig. 8. The difference ratios associated with the various quadrants of interaction tone frequencies are marked with different colors. The d_c ratio value 1 is marked with a red line. The identification of the modes to be investigated in the case of measurement test case *STD_5598_DP* is also shown in Fig. 9 in table form, which are the first three modes in this particular test case.

It has to be noted that no interaction tone has been found for subset *NF*, which confirms the statements in Sec. IV that the *NF* quadrant will not contain a dominant noise source in the case of the present CROR configuration. Therefore, only the three other quadrants have been investigated for the present test case.

As mentioned above in Sec. II A, the PCA modes correspond to modal patterns. These PCA maps are likewise arranged in decreasing order according to their importance in terms of capturing the energy of the acoustic source field. The PCA maps corresponding to the modes identified in Figs. 8 and 9 are shown in Fig. 10. When looking at the PCA maps for the modes identified by the method, it can be seen that there is a clear dominant noise source on each of the PCA maps. Therefore, it can be stated that the method has proven to be successful in the visual separation of the different interaction subgroups into different modes. It can also be seen that the dominant quadrants have been correctly identified for each of the modes, as the PCA maps show that mode 1 is dominated by the *NA*, mode 2 is dominated by the *PA*, and mode 3 is dominated by the *PF* quadrant.

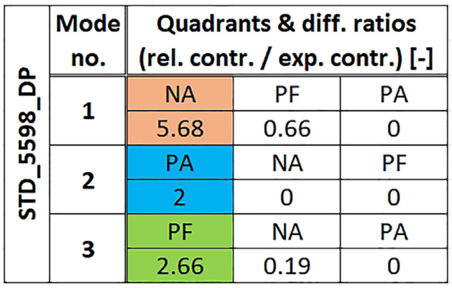

	Mode no.	Quadrants & diff. ratios (rel. contr. / exp. contr.) [-]		
STD_5598_DP	1	NA	PF	PA
		5.68	0.66	0
	2	PA	NA	PF
		2	0	0
	3	PF	NA	PA
		2.66	0.19	0

FIG. 9. The identification of the dominant quadrant of a mode (test case *STD_5598_DP*).

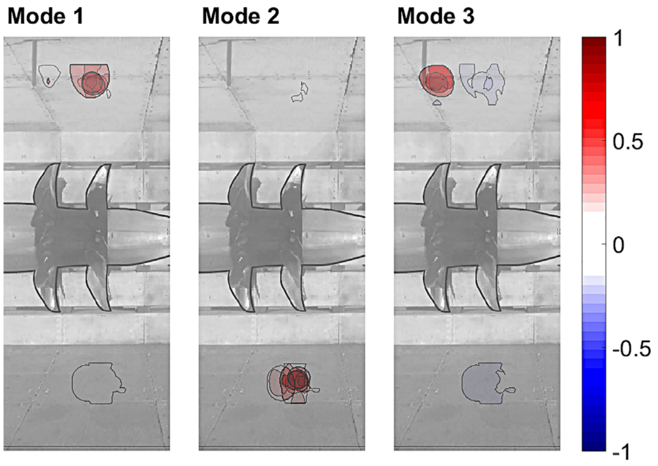

FIG. 10. PCA maps corresponding to the modes identified for test case *STD_5598_DP*.

However, it can also be seen on the PCA maps that aside from the concentrated spots having high values, there are additional spots with much lower values. These are a result of the smaller, but still visible contributions of input beamforming maps containing various noise sources other than that of the dominant ones for the particular modes. Therefore, in order to identify the frequency bins (and consequently the beamforming maps) that are dominated by the designated quadrants of the interaction tone noise sources, a deeper investigation of the weighting coefficients ($\mathbf{a}_j^i$) of the CPOD process is necessary. The weighting coefficients have been presented previously in Eq. (8) in Sec. II A. They give information with regard to the contribution of one particular input beamforming map to the modes, and also with regard to the contributions of the beamforming maps to one particular mode. The larger the value of the weighting coefficient, the larger the impact.

Therefore, by examining the three columns of the $\mathbf{a}_j^i$ matrix pertaining to each modes identified for investigation, information can be gained about how each of the input beamforming maps has contributed to those modes. The weighting coefficients of the beamforming maps pertaining to these modes plotted against their map numbers can be seen in subplot *a*) of Fig. 11. It shows the contributions of the modes to the individual maps. The weighting coefficients are presented in a dimensionless form; that is, every weighting coefficient value has been divided with the value of the largest weighting coefficient for each of the modes. As the goal is to investigate how much impact a beamforming map has on a mode, the beamforming maps pertaining to each of the three modes are to be sorted in descending order according to their weighting coefficients, as can be seen in

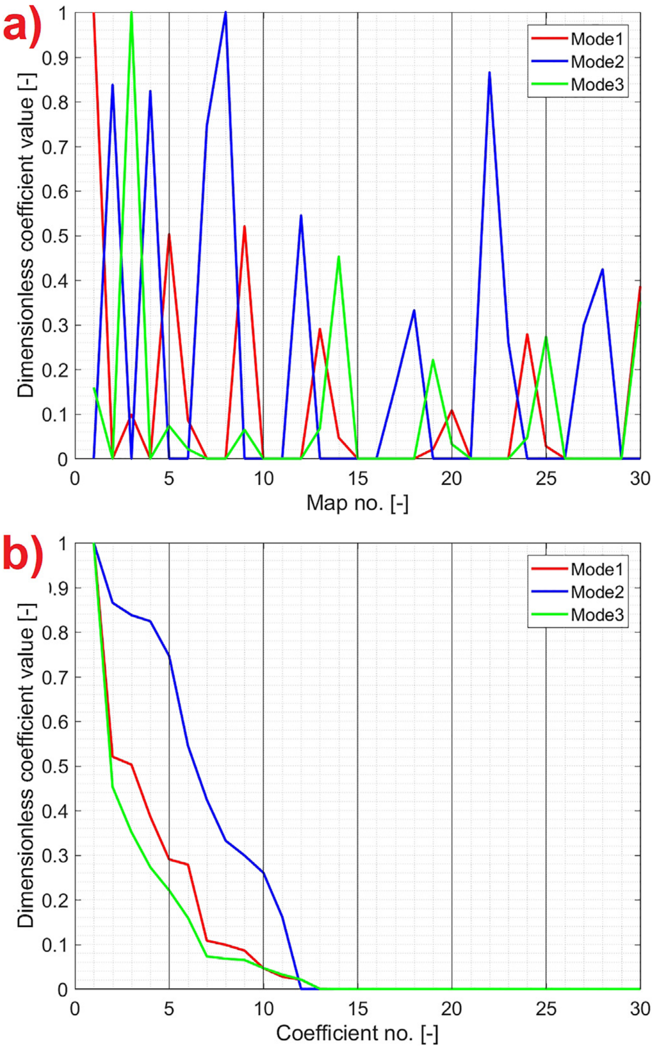

FIG. 11. Weighting coefficients corresponding to the identified modes of test case *STD_5598_DP*: (a) plotted against their map numbers; and (b) sorted in descending order according to their weighting coefficients.

subplot (b) of Fig. 11 (see also step 11 in Fig. 6). Then, only the beamforming maps with non-zero weighting coefficients are to be considered for further investigations (see step 12 in Fig. 6). In the next part of the analysis, the modes considered for each of the subgroups are to be investigated in order to identify the beamforming maps for which the interaction tone noise of a given quadrant is dominant (see step 13 in Fig. 6).

The list of the beamforming maps identified by the automated method for which the interaction tone noise of a given quadrant is dominant can be found in Fig. 12. The dimensionless weighting coefficients, together with the map numbers of the input beamforming maps associated with them, are given for each of the modes. The dimensionless weighting coefficients can be found in the upper, while the map numbers can be found in the lower rows after the mode number and the name of the identified dominant quadrant. The numbers of the maps that have weighting coefficient values of zero can be found at the end of each of the rows with their cells marked with yellow color. These maps are to be excluded from the identification process as they have no contribution to the examined mode. It can be seen that some of the map numbers have been colored gray. The interaction tone noise pertaining to the related quadrant of these beamforming maps have also been identified by the method as not dominant. The logical algorithm of the quadrant identification process can be seen from step 14 in the flow chart of Fig. 6.

It has to be kept in mind that in the case of mode 1 (dominated by the *NA* quadrant) and mode 3 (dominated by the *PF* quadrant), non-zero difference ratios, which are below 1, have been also found for nondominant quadrants. This indicates that some input maps other than the ones corresponding to the dominant subset have also had some effect of minor importance for the given modes. The first question to be answered before categorizing a beamforming map is whether a particular beamforming map has been previously identified as a dominant interaction tone map for a higher order weighting coefficient of another mode (starting from the left-hand side of the rows), as can be seen in step 14) in the flow chart of Fig. 6. If it has, then the interaction tone noise pertaining to the related quadrant of this beamforming map is not dominant, and the color of the map is to be set to gray, that is, excluding the map from the analysis (see step 15/a in Fig. 6) of that particular quadrant. An example for this case (see Fig. 12) is map No. 3, which has been previously identified as a dominant interaction tone map pertaining to the *PF* quadrant for the first largest weighting coefficient of mode 3. Consequently, it cannot be identified as a dominant interaction tone map pertaining to the eighth largest weighting coefficient of mode 1 (*NA* quadrant); therefore, it is to be excluded as pertaining to the investigation of the *NA* quadrant. Another example is map No. 1, which also had to be excluded from the identification process in the case of the sixth largest weighting coefficient of mode 3, as it has already been identified as a dominant interaction tone map pertaining to mode 1 (see weighting coefficient no. 1).

On the other hand, if the beamforming map has not been previously identified as a dominant interaction tone map for a higher order weighting coefficient of another mode (starting from the left-hand side of the rows), then it should be examined whether the same map number is present for a weighting coefficient of the same order for another mode that is under investigation (see step 15/b in Fig. 6). If it is, then the dimensionless values of their weighting coefficients have to be compared. The interaction tone noise source is dominant, as pertaining to the related quadrant of the beamforming map for which the dimensionless value of the weighting coefficient of the same order is the largest (see step 16/a in Fig. 6). However, if the same map number is not present for a weighting coefficient of the same order for another considered mode, then it can be stated that the interaction tone noise pertaining to the related quadrant of that beamforming map is a dominant one (see step 16/b in Fig. 6).

As a result of the quadrant identification process, it has been identified using a fully automated process whether a beamforming map pertaining to a frequency bin at an interaction tone frequency is indeed dominated by an interaction tone noise source or not. Furthermore, the dominant interaction tone quadrants have also been determined with the method for each of the identified maps. Figure 13 shows the BFpeak spectrum of measurement test case *STD_5598_DP* together with the interaction tone noise sources categorized by their

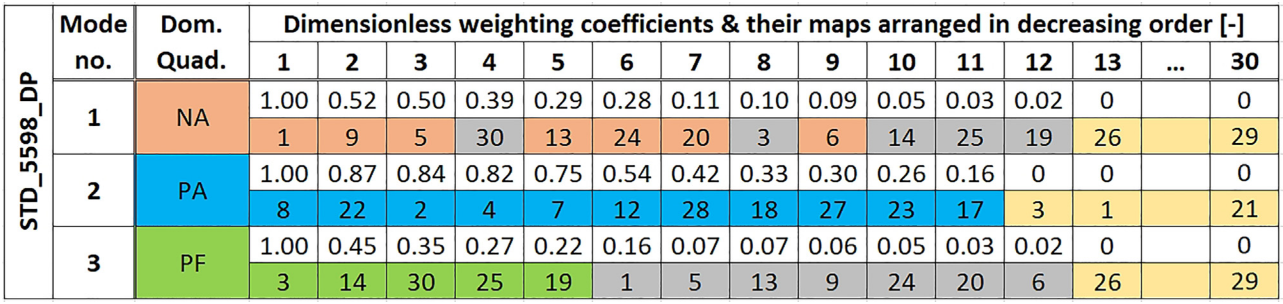

	Mode no.	Dom. Quad.	Dimensionless weighting coefficients & their maps arranged in decreasing order [-]														
			1	2	3	4	5	6	7	8	9	10	11	12	13	...	30
STD_5598_DP	1	NA	1.00	0.52	0.50	0.39	0.29	0.28	0.11	0.10	0.09	0.05	0.03	0.02	0		0
			1	9	5	30	13	24	20	3	6	14	25	19	26		29
	2	PA	1.00	0.87	0.84	0.82	0.75	0.54	0.42	0.33	0.30	0.26	0.16	0	0		0
			8	22	2	4	7	12	28	18	27	23	17	3	1		21
	3	PF	1.00	0.45	0.35	0.27	0.22	0.16	0.07	0.07	0.06	0.05	0.03	0.02	0		0
			3	14	30	25	19	1	5	13	9	24	20	6	26		29

FIG. 12. The identified dominant quadrants and their beamforming maps for test case *STD_5598_DP*.

respective quadrants into frequency bins using the automated method of the present study. The BFpeak spectrum is marked by black color, while for the vertical lines pertaining to the frequency bins of the identified interaction tone quadrants, the same colors are used as previously in Figs. 9 and 12.

VI. RESULTS FOR THE ANALYSES OF THE VARIOUS CROR DATASETS

In the present section, in order to test the robustness of the proposed method, the analysis has been carried out on four additional measurement test cases (see Fig. 1), for which the results will be presented, then the five test cases will be compared to each other. The results of the robustness tests are visualized using the BFpeak spectra of the measurement test cases together with their identified interaction tone noise sources categorized according to their respective quadrants, as can be seen in Figs. 14–17.

Based on the data presented in Figs. 13–17, the main source of noise generation (i.e., the potential flow field, or a combination of potential flow field and viscous wake) can be identified from the quadrant into which a particular interaction tone falls (see more details in Sec. IV). A considerable advantage of the method apart from being able to identify and subsequently categorize frequency bins pertaining to the quadrants of interaction tones is that it is also capable of identifying the frequency bins of the beamforming maps for which the interaction tone noise is not dominant. Consequently, each of the measurement test cases presented in Figs. 13–17 is having a different number of interaction tone quadrants identified.

It can also be seen that peaks aside from the ones associated with interaction tones are also present in the spectra. These peaks are the result of additional kinds of tonal noise sources present in the dataset, such as blade passing frequency noise and shaft order noise (see more details in Refs. 12 and 24–26) It can be concluded that the method has been correct in not identifying these frequency bins as interaction tone dominated.

The validation of the results has also been performed in order to provide evidence regarding the accuracy of the proposed automated analysis. Therefore, the five datasets have also been processed by manual sorting and categorization according to the method presented by Fenyvesi *et al.*,[12] and then, it has been checked whether the results of the manual categorization agree with those of the automated method. It has been concluded that for the five measurement test cases investigated herein, a total of six deviations have been found. In the case of measurement test case *STD_5598_DP*, all interaction tone frequency bins and their respective quadrants have been correctly identified.

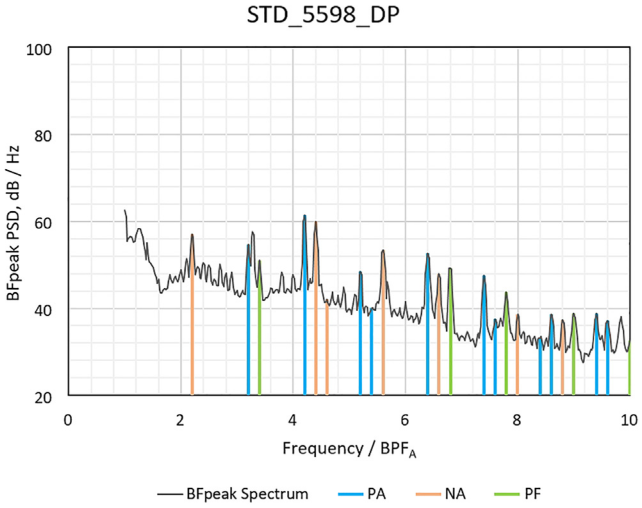

FIG. 13. BFpeak PSD spectrum of test case *STD_5598_DP*, colored according to the quadrant of each identified dominant interaction tone noise source test case.

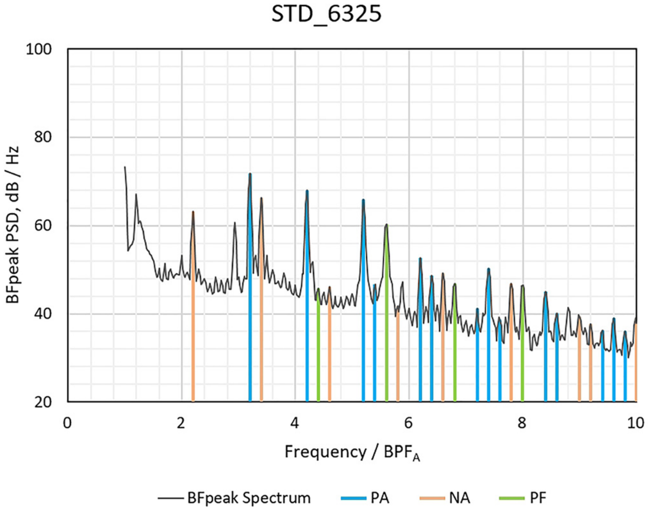

FIG. 14. BFpeak PSD spectrum of test case *STD_6325*, colored according to the quadrant of each identified dominant interaction tone noise source test case.

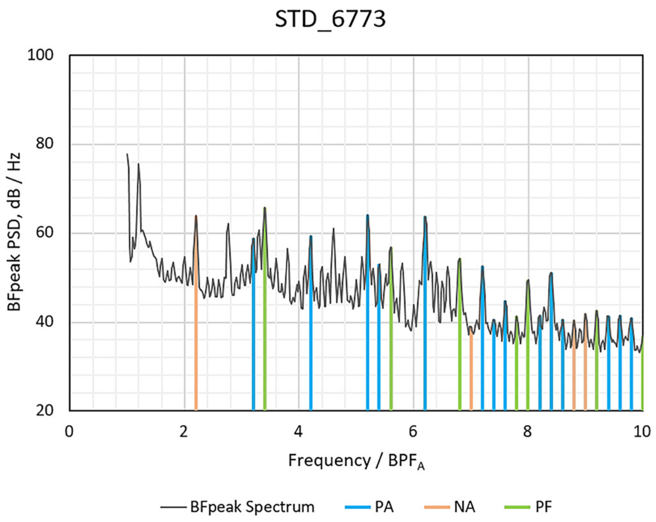

FIG. 15. BFpeak PSD spectrum of test case *STD*_6773, colored according to the quadrant of each identified dominant interaction tone noise source test case.

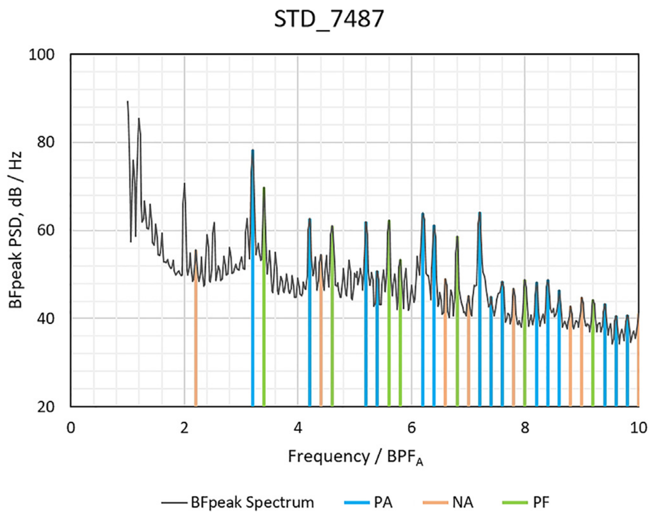

FIG. 17. BFpeak PSD spectrum of test case *STD*_7487, colored according to the quadrant of each identified dominant interaction tone noise source test case.

As for measurement test cases *STD*_6325 and *STD*_7245, one deviation per test case has been found, while for measurement test cases *STD*_6773 and *STD*_7487, two deviations per test case have been found. All of the six deviations have been thoroughly examined, and it has been concluded that the main reason behind all of them has been the substantial spatial interference of broadband noise sources, background noise, and sidelobes contained in the input measurement datasets. Example maps for both kinds of interferences are shown in Fig. 18. In subplot (a) of Fig. 18, the interference of broadband noise sources, while in subplot (b) of Fig. 18, the interference of background noise and sidelobes can be observed. It can be seen on the maps for both examples that some parts of the dominant noise sources can be found in the immediate vicinity of the Mach radius while no noise source having the characteristics of an interaction noise source can be found on the map, which can influence the results in the case of a few input maps. Nonetheless, it has also been found that the beamforming maps for which the deviations have been observed have all been the least significant contributors of their respective modes.

When examining the results for the various CROR test cases, it can also be observed that the amplitudes of the spectra have increased with increasing the *RPM* of the rotors. In Fig. 19(a) summary as pertaining to the number of interaction tones identified in each quadrant per measurement test case are presented together with the expected values determined prior to the CPOD analyses of the datasets. It can

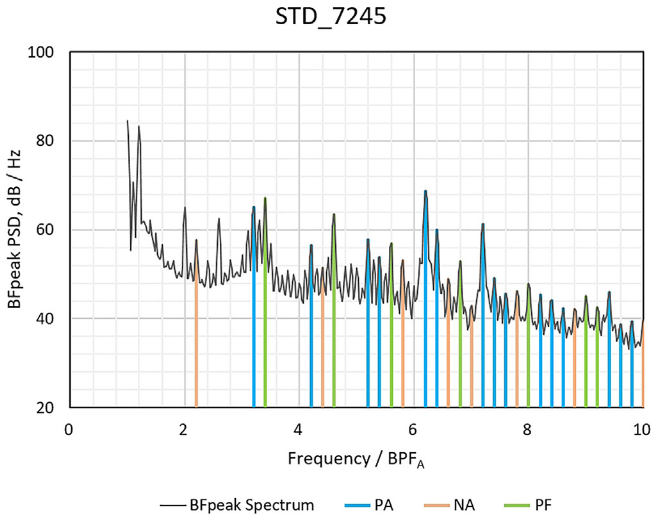

FIG. 16. BFpeak PSD spectrum of test case *STD*_7245, colored according to the quadrant of each identified dominant interaction tone noise source test case.

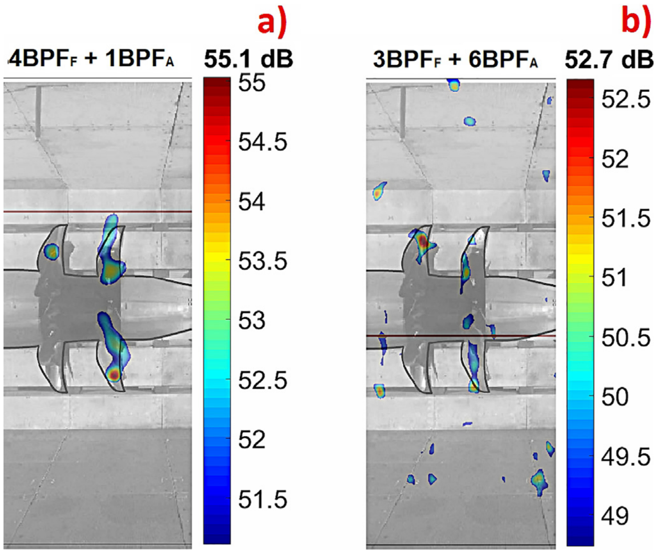

FIG. 18. Spatial interference of broadband noise sources (a) and as well as background noise and sidelobes (b).

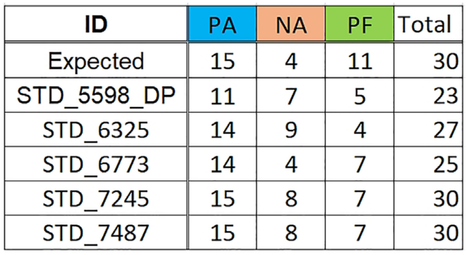

ID	PA	NA	PF	Total
Expected	15	4	11	30
STD_5598_DP	11	7	5	23
STD_6325	14	9	4	27
STD_6773	14	4	7	25
STD_7245	15	8	7	30
STD_7487	15	8	7	30

FIG. 19. The number of interaction tone quadrants identified per measurement test case together with the expected values.

be seen that the largest number of identified quadrants are associated with the beamforming maps of the positive aft quadrant, the second largest contributor is the negative aft quadrant for most of the test cases, and the least number of identified quadrants are associated with the positive forward quadrant. Another interesting finding is that the numbers do not always match the values of the expected contributions, the main difference being the number of maps identified as dominated by the *NA* and *PF* quadrants. The reason behind this can be that the viscous wake of the forward rotor could have had an effect, which is larger than expected on the noise sources associated with the aft rotor. The above difference also highlights the importance of the automated method used herein for the correct identification of interaction tone noise sources. Furthermore, it can also be seen that with increasing the *RPM*, the total number of interaction tone quadrants identified per test case have increased, even up to the total number of beamforming maps considered for investigation in the case of the two largest *RPM*s. Therefore, it can be concluded that the increase in the *RPM* has raised the tonal noise sources farther out of the broadband, making them easier to identify.

Finally, it can be concluded that the proposed automated method has proven to be a powerful and effective tool for decreasing the time needed for the analysis and categorization of interaction tone noise sources as compared to the manual sorting method by several orders of magnitude, as it only takes a few minutes to complete. On the contrary, the manual sorting method[12] could take from many hours up to one day to complete even for a highly experienced analyst.

VII. CONCLUSION

An automated method has been presented for the investigation of the interaction tone noise of counter-rotating rotors. The quick, objective, and easy-to-use analysis of these significant noise sources highly contributes to the better understanding, efficient development, and subsequent noise reduction of counter-rotating rotor configurations. This opens the door for a wide range of industrial applications of which the two most significant are unmanned aerial vehicles and counter-rotating open rotor aircraft engines. Following a detailed description of the proposed method, principal component analysis and common-base proper orthogonal decomposition has been used to analyze five datasets of beamforming noise source maps of a counter-rotating open rotor at five different RPMs. Four subcategories of counter-rotating open rotor interaction noise have been determined, which can be directly associated with different noise generating mechanisms. Then, dominant beamforming maps pertaining to each category have been identified. It has been found that for the examined test cases, the viscous wake of the forward rotor could have had an effect which is larger than expected on the noise sources associated with the aft rotor. It has also been found that while the increase in the *RPM* of the rotors have caused an increase in the overall amplitude of the noise, the amplitudes of interaction tone noise sources have been raised farther out of the broadband. It has been concluded that a very significant advantage of the proposed automated method is that the time needed for the analysis and categorization of interaction tone noise sources of large datasets can be decreased by several orders of magnitude as compared to manual sorting. Furthermore, the results of the automated method are easy to comprehend and it can even be used by a relatively inexperienced analyst as it only requires one to feed general information about the counter-rotating dataset into the algorithm without the need to use subjective judgment during the process.

ACKNOWLEDGMENTS

The testing of the CROR was funded by the Environmentally Responsible Aviation Project of the NASA Integrated Systems Research Program and the Fixed Wing Project of the NASA Fundamental Aeronautics Program. The research presented in this paper has been supported by the Hungarian National Research, Development and Innovation Centre under Contract No. K 129023, the János Bolyai Research Scholarship of the Hungarian Academy of Sciences, and the NRDI Funds (TKP2020 NC, Grant No. BME-NCS and TKP2021, Project No. BME-NVA-02) based on the charter of bolster issued by the NRDI Office under the auspices of the Ministry for Innovation and Technology. The authors acknowledge financial support from the DAAD Eastern Partnership (2019–2021) and the TKA-DAAD Programmes for Project-Related Personal Exchange (PPP) (2022–2023).

AUTHOR DECLARATIONS

Conflict of Interest

The authors have no conflicts to disclose.

DATA AVAILABILITY

The data that support the findings of this study are available from the corresponding author upon reasonable request.

REFERENCES

[1] H. H. Hubbard, “Sound from dual-rotating and multiple single-rotating propellers,” Report No. NACA-TN-1654 (NACA, 1948).
[2] W. Strack, G. Knip, A. Weisbrich, J. Godston, and E. Bradley, “Technology and benefits of aircraft counter rotation propellers,” Report No. NASA TM 82983 (NASA, 1981).
[3] D. B. Hanson, “Noise of counter-rotation propellers,” J. Aircraft **22**, 609–617 (1985).
[4] R. Parker and M. Lathoud, “Green aeroengines: Technology to mitigate aviation impact on environment,” Proc. Inst. Mech. Eng., Part C **24**, 529–538 (2010).
[5] L. S. Langston, “Open rotor engines-still an open question?,” Mech. Eng. **140**, S46–S48 (2018).
[6] R. P. Woodward, “Noise of a model high speed counterrotation propeller at simulated takeoff/approach conditions (F7/A7),” in *11th Aeroacoustics Conference*, Sunnyvale, CA (National Aeronautics and Space Administration; National Technical Information Service, distributor, 1987) pp. 1–25.
[7] V. Blandeau, “Aerodynamic broadband noise from contra-rotating open rotors,” Ph.D. thesis (University of Southampton, 2011).
[8] V. P. Blandeau, P. F. Joseph, M. J. Kingan, and A. B. Parry, “Broadband noise predictions from uninstalled contra-rotating open rotors,” Int. J. Aeroacoust. **12**, 245–281 (2013).

[9] D. E. Van Zante, J. A. Gazzaniga, D. M. Elliott, and R. P. Woodward, "An open rotor test case: F31/A31 historical baseline blade set," in *20th International Symposium on Airbreathing Engines Gothenburg, Sweden, 12-16 September, 2011* (ISABE, 2011), pp. 2011–1310.

[10] C. Horváth, E. Envia, and G. G. Podboy, "Limitations of phased array beamforming in open rotor noise source imaging," AIAA J. **52**, 1810–1817 (2014).

[11] Cs. Horváth, "Beamforming investigation of dominant counter-rotating open rotor tonal and broadband noise sources," AIAA J. **53**, 1602–1611 (2015).

[12] B. Fenyvesi, K. Tokaji, and C. Horváth, "Investigation of a pylons effect on the character of counter-rotating open rotor noise using beamforming technology," Acta Acust. Acust. **105**, 56–65 (2019).

[13] D. Smith, A. Filippone, and N. Bojdo, "Noise reduction of a counter rotating open rotor through a locked blade row," Aerosp. Sci. Technol. **98**, 105637 (2020).

[14] R. S. McKay, S. T. Go, S. Jung, and M. J. Kingan, "Noise from unmanned aerial vehicle contra-rotating propellers," J. Phys.: Conf. Ser. **1909**, 012008 (2021).

[15] A. Parry and D. Crighton, "Prediction of counter-rotation propeller noise," AIAA Paper No. 89-1141, 1989.

[16] M. Kingan and P. Sureshkumar, "Open rotor centrebody scattering," J. Sound Vib. **333**, 418–433 (2014).

[17] D. Elliott, "Initial investigation of the acoustics of a counter rotating open rotor model with historical baseline blades in a low speed wind tunnel," AIAA Paper No. 2011-2760, 2012.

[18] A. B. Parry and S. Vianello, "A project study of open rotor noise," Int. J. Aeroacoust. **11**, 247–258 (2012).

[19] G. Delattre and F. Falissard, "Influence of torque ratio on counter-rotating open-rotor interaction noise," AIAA J. **53**, 2726–2738 (2015).

[20] C. Horváth, "Investigating counter-rotating open rotor noise sources from a broadband point of view," in *Proceedings on CD of the 5th Berlin Beamforming Conference* (Berlin Beamforming Conference, 2014), pp. 1–14.

[21] K. Tokaji, B. Soós, and C. Horváth, "Extracting the broadband noise sources of counter-rotating open rotors," AIAA Paper No. AIAA 2019-2572, 2019.

[22] K. Tokaji, B. Soós, and C. Horváth, "Beamforming method for extracting the broadband noise sources of counter-rotating open rotors," AIAA J. **58**, 3028–3039 (2020).

[23] K. Tokaji and C. Horváth, "Effect of a pylon on the broadband noise sources of counter-rotating turbomachinery," Int. J. Aeroacoust. **20**, 979–1002 (2021).

[24] B. Fenyvesi, J. Kriegseis, and C. Horváth, "Application of a combined method for the investigation of turbomachinery noise sources: Beamforming and proper orthogonal decomposition," AIAA Paper No. AIAA 2019-2637, 2019.

[25] B. Fenyvesi, J. Kriegseis, and C. Horváth, "Investigation of rotating coherent BPF noise sources via the application of beamforming and proper orthogonal decomposition," in *INTER-NOISE and NOISE-CON Congress and Conference Proceedings, InterNoise19, Madrid, Spain* (INTER-NOISE and NOISE-CON Congress and Conference, 2019), pp. 3127–3138.

[26] B. Fenyvesi and C. Horváth, "Identification of turbomachinery noise sources via processing beamforming data using principal component analysis," Period. Polytech., Mech. Eng. **66**, 32–19 (2021).

[27] J. Antoni, Q. Leclère, A. Dinsenmeyer, E. Julliard, S. Bouley, C. Picard, and P. Sijtsma, "Standalone extraction of tonal components from aeroacoustic signals," AIAA J. **60**, 844–859 (2022).

[28] J. Antoni, Q. Leclère, A. Dinsenmeyer, E. Julliard, S. Bouley, C. Picard, and P. Sijtsma, "Stand-alone extraction of cyclostationary broadband components from aeroacoustic signals," AIAA J. **60**, 1817–1832 (2022).

[29] V. K. Lakshminarayan and J. D. Baeder, "Computational investigation of microscale coaxial-rotor aerodynamics in hover," J. Aircraft **47**, 940–955 (2010).

[30] S. Prior and J. Bell, "Empirical measurements of small unmanned aerial vehicle co-axial rotor systems," J. Sci. Innovation **1**, 1–18 (2011); available at https://eprints.soton.ac.uk/342834/.

[31] D. Shukla and N. Komerath, "Drone scale coaxial rotor aerodynamic interactions investigation," J. Fluids Eng. **141**, 071106 (2019).

[32] M. Y. Zakaria, A. F. Nemnem, K. Gad, and M. M. Abdelwahab, "Performance analysis and aerodynamic modeling of contra-rotating ducted fan UAV," AIAA Paper No. AIAA 2019-1788, 2019.

[33] S. Deng, S. Wang, and Z. Zhang, "Aerodynamic performance assessment of a ducted fan UAV for VTOL applications," Aerosp. Sci. Technol. **103**, 105895 (2020).

[34] Z. Liu, C. Bu, X. Kong, D. Yang, and B. Li, "Computational investigation of noise interaction for a nano counter-rotating rotor in a static condition," Int. J. Comput. Mater. Sci. Eng. **07**, 1850004 (2018).

[35] S. Darvishpoor, J. Roshanian, A. Raissi, and M. Hassanalian, "Configurations, flight mechanisms, and applications of unmanned aerial systems: A review," Prog. Aerosp. Sci. **121**, 100694 (2020).

[36] R. S. McKay, M. J. Kingan, S. T. Go, and R. Jung, "Experimental and analytical investigation of contra-rotating multi-rotor UAV propeller noise," Appl. Acoust. **177**, 107850 (2021).

[37] C. Horváth, B. Fenyvesi, and B. Kocsis, "Drone noise reduction via radiation efficiency considerations," in Conference on Modelling Fluid Flow (CMFF'18) (2018).

[38] R. P. Dougherty, "Beamforming in acoustic testing," in *Aeroacoustic Measurements*, edited by T. J. Mueller (Springer, Berlin/Heidelberg, 2002), pp. 62–97.

[39] K. Karhunen, "Zur spektraltheorie stochasticher prozesse," Ann. Acad. Sci. Fenn., Ser. A **37**, 1–7 (1946); available at https://books.google.hu/books?id=X3F3SwAACAAJ.

[40] M. Loève, *Probability Theory* (Van Nostrand, New York, 1955).

[41] J. L. Lumley, "The structure of inhomogeneous turbulent flows," in *Atmospheric Turbulence and Radio Wave Propagation*, edited by A. Yaglom and V. Takarski (Nauka, Moskow, 1967), pp. 166–178.

[42] S. A. M. Stein, A. E. Loccisano, S. M. Firestine, and J. D. Evanseck, "Chapter 13 principal components analysis: A review of its application on molecular dynamics data," Annu. Rep. Comput. Chem. **2**, 233–261 (2006).

[43] R. W. Preisendorfer and C. D. Mobley, *Principal Component Analysis in Meteorology and Oceanography* (Elsevier, Amsterdam/New York/Oxford, 1988), p. 425.

[44] K. E. Meyer, J. M. Pedersen, and O. Özcan, "A turbulent jet in crossflow analysed with proper orthogonal decomposition," J. Fluid Mech. **583**, 199–227 (2007).

[45] G. Berkooz, P. Holmes, and J. L. Lumley, "The proper orthogonal decomposition in the analysis of turbulent flows," Annu. Rev. Fluid Mech. **25**, 539–575 (1993).

[46] S. A. Glegg, W. J. Devenport, N. J. Molinaro, and W. N. Alexander, "Proper orthogonal decomposition and its use in the analysis of fluid structure interaction noise," AIAA Paper No. AIAA 2018-3787, 2018.

[47] S. Liang, W. Chen, R. P. Liem, and X. Huang, "Experimental analysis of cooling fan noise by wavelet-based beamforming and proper orthogonal decomposition," IEEE Access **8**, 121197–121203 (2020).

[48] J. Kriegseis, T. Dehler, M. Gnirß, and C. Tropea, "Common-base proper orthogonal decomposition as a means of quantitative data comparison," Meas. Sci. Technol. **21**, 085403 (2010).

[49] G. Zambonini, X. Ottavy, and J. Kriegseis, "Corner separation dynamics in a linear compressor cascade," J. Fluids Eng. **139**, 061101 (2017).

[50] J. Kriegseis, T. Dehler, M. Pawlik, and C. Tropea, "Pattern-identification study of the flow in proximity of a plasma actuator," AIAA Paper No. 2009-1001, 2009.

[51] A. Chatterjee, "An introduction to the proper orthogonal decomposition," Curr. Sci. **78**, 808–817 (2000); avaialable at http://www.jstor.org/stable/24103957.

[52] J. Weiss, "A tutorial on the proper orthogonal decomposition," AIAA Paper No. 2019-3333, 2019.

[53] N. Aubry, "On the hidden beauty of the proper orthogonal decomposition," Theor. Comput. Fluid Dyn. **2**, 339–352 (1991).

[54] C. E. Tinney, "Sparse biorthogonal decomposition," AIAA Paper No. 2021-1851, 2021.

[55] L. Cordier, J.-P. Bonnet, and J. Delville, "Proper orthogonal decomposition: POD," in *Springer Handbook of Experimental Fluid Mechanics*, edited by C. Tropea, A. L. Yarin, and J. F. Foss (Springer, Heidelberg, 2007), pp. 1346–1398.

[56] R. P. Dougherty, "Functional beamforming for aeroacoustic source distributions," AIAA Paper No. AIAA 2014-3066, 2014.

[57] E. Envia, "Open rotor aeroacoustic modelling," Report No. NASA TM 2012-217740 (NASA, 2012).

[58] S. Anupam and C. Hsuan-nien, "Prediction of aerodynamic tonal noise from open rotors," J. Sound Vib. **332**, 3832–3845 (2013).

[59] C. Wang and L. Huang, "Theoretical acoustic prediction of the aerodynamic interaction for contra-rotating fans," AIAA J. **56**, 1855–1866 (2018).